Letters

Effects of External DC *B*-Fields on High-Frequency Impedance Characteristics of Multilayer Ceramic Capacitors

Rongrong Zhang, *Student Member, IEEE*, Chaoqiang Jiang, *Senior Member, IEEE*, Shuo Wang, *Fellow, IEEE*, Teng Long, *Member, IEEE*, Atif Iqbal, *Fellow, IEEE*, Jian Qiu, Cheng Wang, Kefu Liu, *Member, IEEE*, and Hui Zhao, *Senior Member, IEEE*

***Abstract*—Multilayer ceramic capacitors (MLCCs) are widely used in power electronics. Because paraelectric and ferroelectric material are nonmagnetic dielectrics, *B*-field effects are typically ignored in datasheets and design consideration. This letter reveals a significant, previously undocumented phenomenon: *B*-fields cause substantial high-frequency impedance variation in MLCCs, with observed changes exceeding 43% under *B*-fields up to 491 mT. Supplementary material includes all the design files for the measurement kit and all the raw data to ensure reproducibility. Raman spectroscopy and microstructure were employed to characterize the material composition and physical structure of the MLCCs.**

***Index Terms*—*B*-field, ferroelectric material, high-frequency impedance, multilayer ceramic capacitor, paraelectric material.**

I. Introduction

MULTILAYER ceramic capacitors (MLCCs) are essential and widely used in power electronics, for chip decoupling, powering gate drivers, switched-capacitor converters, and resonant converters [1], [2], [3], [4]. Their market value (USD 14.4B [5]) significantly exceeds that of other passive components like inductors (USD 4.5B [6]), underscoring their importance. Furthermore, the significantly higher energy density of capacitors compared to inductors is also driving the increased use of high-capacitance circuitry in low-voltage systems like Point-of-Load converters and data center power supplies.

TABLE I
Factors Affecting MLCC Performance

Factors	Impact	Key reference
DC bias	Capacitance variation, ESR variation	[1, 7]
Large signal	ESR variation, power loss variation	[1, 7, 8]
Temperature	Power loss, capacitance, reliability	[9, 10]
Mechanical stress	Reliability, dielectric constant, dielectric loss, polarization	[11]
B-field	First resonant frequency, high frequency impedance, ESR	This work

As shown in Table I, research on MLCCs mainly investigates their performance under dc bias voltage [1], [4], [7], high current [1], temperature [9], [10], and mechanical stress [11]. However, their performance under *B*-fields is often overlooked. This oversight is mainly because the dielectric materials in MLCCs, predominantly ferroelectric (Class II) or paraelectric (Class I) material [7], are primarily influenced by *E*-fields and are largely unaffected by *B*-field.

However, in modern society, *B*-fields are becoming increasingly prevalent and hard to avoid. Consequently, understanding MLCC performance under *B*-field is becoming critical.

The widespread presence of *B*-field is largely due to the increasing reliance on the modern power electronics. As shown in Table II, electric vehicles (EVs) extensively use permanent magnet (PM) motors. Magnetic Resonance Imaging (MRI) scanners generate intense *B*-fields up to 7.0 T. Devices equipped with MagSafe also incorporate PM with *B* ranging between 40.4 and 98.3 mT.

Shielding dc *B*-fields is inherently more challenging than shielding *E*-fields or ac *B*-field. Effective shielding is readily achieved, at high frequencies using Faraday cages [23] and low frequencies via highly conductive materials and grounding. In contrast, attenuating *B*-fields is considerably challenging. Therefore, investigating MLCC performance variations under such conditions is important.

Received 13 May 2025; revised 17 June 2025 and 5 August 2025; accepted 22 August 2025. Date of publication 27 August 2025; date of current version 23 December 2025. This work is supported by the joint funds of Industryuniversity-research of Shanghai Academy of Spaceflight Technology under Grant SAST2023-050. *(Corresponding author: Hui Zhao.)*

Rongrong Zhang, Jian Qiu, Kefu Liu, and Hui Zhao are with the College of Intelligent Robotics and Advanced Manufacturing, Fudan University, Shanghai 200433, China (e-mail: hui_zhao@fudan.edu.cn).

Chaoqiang Jiang is with the School of Electrical Engineering, City University of Hong Kong, Hong Kong 999077, China.

Shuo Wang is with the Department of Electrical and Computer Engineering, University of Florida, Gainesville, FL 32611-6200 USA.

Atif Iqbal is with the Department of Electrical Engineering, Qatar University, Doha, Qatar.

Cheng Wang is with the Nanjing University of Science and Technology, Nanjing 210094, China.

Teng Long is with the Department of Engineering, University of Cambridge, CB3 0FA Cambridge, U.K.

This article has supplementary material provided by the authors and color versions of one or more figures available at https://doi.org/10.1109/TPEL.2025.3603392.

Digital Object Identifier 10.1109/TPEL.2025.3603392

TABLE II
B-FIELD MAGNITUDE IN VARIOUS APPLICATIONS

Field type	Application	Magnetic field source	*B*-field magnitude	Key reference
DC	Electric vehicles	PMs	> 1.0 T	[12, 13]
	iPhone 12	PMs	40.4 mT	[14]
	Apple watch 6	PMs	98.3 mT	[14]
	MRI	Superconducting magnets	1.5-7.0 T	[15, 16]
AC	Switched-mode power supplies	Power inductor / transformer	≤ 10.0 μT	[17–19]
	Wireless power transfer	Transmitter (Tx) / Receiver (Rx) coils	≤ 800.0 μT	[20] [21] [22]

This comparison demonstrates two critical disadvantages of the conventional impedance adapter solution: 1) an elevated noise floor compared to the shunt-through method; and 2) a strong vulnerability to external *B*-fields, which further degrades its noise performance. This clearly supports using the shunt-through technique for minimizing noise and mitigating *B*-field interference in impedance measurements.

Our work reveals a previously unrecognized dependence of MLCC high-frequency impedance to external *B*-fields. Our data demonstrate impedance variations exceeding 43% under external *B*-fields. This dependence is absent from current datasheets and prior studies. Therefore, engineers are likely to overlook it, which can lead to impedance mismatching, EMI filter's performance degrading, and resonant frequency shifting.

To ensure experimental reproducibility, we have systematically discussed the design considerations of our experiments, and comprehensively discussed the influence of *B*-field magnitude and direction on the capacitance's impedance. A kit was designed to avoid the impact of external mechanical stress and other confounding variables. The conclusions demonstrate universality across Class I and Class II MLCC, various package sizes, different manufacturers, and diverse capacitance values. We include all design files and all the raw experimental data to provide reproducibility and strong support for our findings' validation.

II. DESIGN OF EXPERIMENT

A. Review on Existing Characterization Methods

The review of capacitor characterization helps us understand and aligns the principles, considerations, and targets for the design of our characterization measurements under *B*-field.

The challenge in existing capacitor characterization is typically lies in how to design setups to apply an external dc voltage while ensuring the setup method has minimal impact on the measurement. Refs. [4], [24], [25] use transformers to apply dc voltage, which limits the total effective measurement bandwidth due to the transformer's bandwidth. Ref. [1] uses multilevel resonant circuit to introduce the dc voltage, but the circuit is complicated. Furthermore, precision is limited by the measurement instruments such as power meters [26]. To minimize the influence of auxiliary circuits, recent advances have focused on alternative characterization approaches. In 2023, Coday and

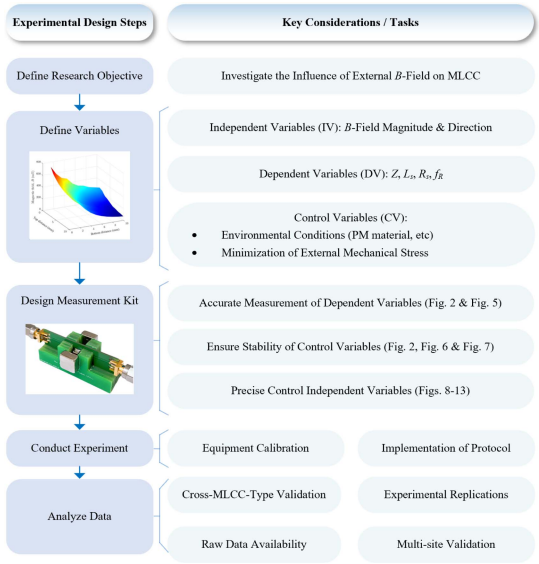

Fig. 1. Principles, workflows, and key considerations for experimental design.

Pilawa-Podgurski [7] employed calorimetric methods to obtain accurate power loss and ESR data, effectively bypassing some of the traditional measurement limitations. Menzi et al. [8] addressed the challenge of peak-charge measurement difficulties by proposing a simplified ESR-based model that achieves reasonably accurate results without requiring peak charge measurements. In addition, Zakzewski et al. [27] recognized that nonlinear effects can cause waveform distortion and proposed a compensation method to correct for these distortions.

Characterization targets high-frequency properties including Z, f_R, *ESR*, and *ESL*. Although the independent variables differ, the dependent variables, measurement methods, controlled variables, and evaluation techniques from electrical characterization are highly relevant with our experimental design.

B. Key Considerations for Experimental Design

Based on experimental design principles [28], the experimental setup needs to ensure reliable, precise, repeatable, and reproducible measurements of MLCC characteristics. Therefore, experimental design steps and key considerations are presented in Fig. 1.

Based on experimental design principles [28], the experimental setup needs to ensure reliable, precise, repeatable, and reproducible measurements of MLCC characteristics. Therefore, experimental design steps and key considerations are presented in Fig. 1.

C. Measurement Accuracy

Conventional impedance analyzers face challenges in accurately measuring low (mΩ-level) impedance. For example, the recommended impedance range for the Bode 100 in Fig. 2(a) is above 20 mΩ, while for the Keysight E4990A, the limit is above 25 mΩ. To address this limitation, we employ the shunt-through method based on a network analyzer, as illustrated in Fig. 2(b). This method allows for accurate measurements down to approximately 1 mΩ.

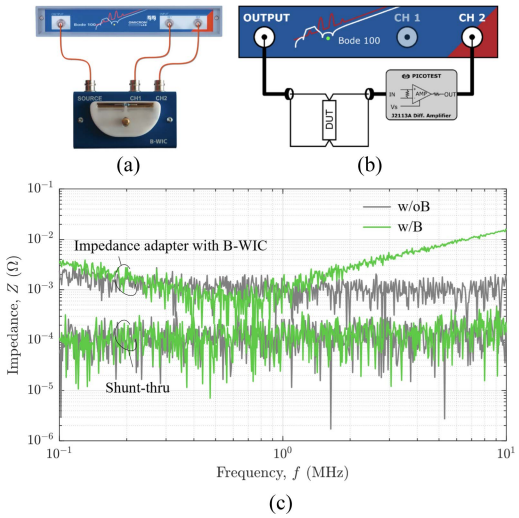

Fig. 2. Comparison of impedance noise floor for: (a) An impedance adapter with B-WIC and (b) a shunt-through setup. (c) Compares the results of both setups, under conditions with (w/B) and without (w/o B) an external *B*-field.

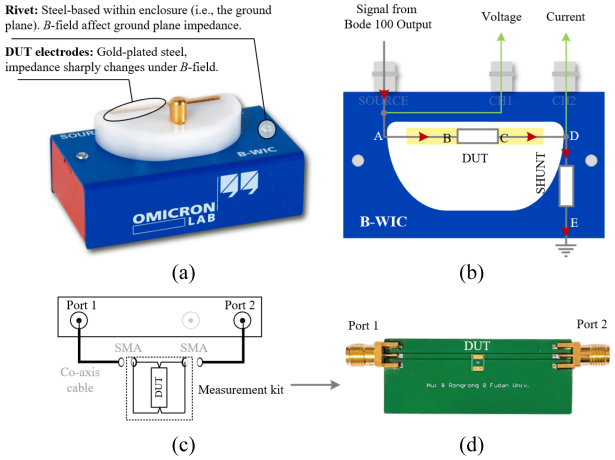

Fig. 3. Comparison of the conventional impedance adaptor and proposed shunt-through measurement setups: (a) The conventional setup highlighting ferromagnetic components susceptible to *B*-field interference, (b) the conventional schematics, (c) the block diagram of the proposed shunt-through configuration, and (d) the proposed custom-designed test fixture with only nonmagnetic components.

Shunt-through method is based on transmission parameter (S_{21}) characterization, which represents the ratio of the signal arriving at Port 2 to the signal leaving Port 1. The relationship between S_{21} and the impedance of the DUT is as follows:

$$Z_{DUT} = Z_0 S_{21} / (2(1 - S_{21})) \tag{1}$$

where

Z_{DUT} is the complex impedance of the MLCC;

$Z_0 = 50\,\Omega$ is the characteristic impedance of the measurement system (50 Ω).

Based on (1), the sensitivity analysis can be derived as Fig. 4, showing the shunt-through method's high sensitivity for resolving low impedance values.

A comparison of the noise floors in Fig. 2(c) demonstrates that the shunt-through technique effectively minimizes noise and ensures measurement accuracy. Fig. 5 further analyzes the mechanism of noise floor degradation in the conventional setup and

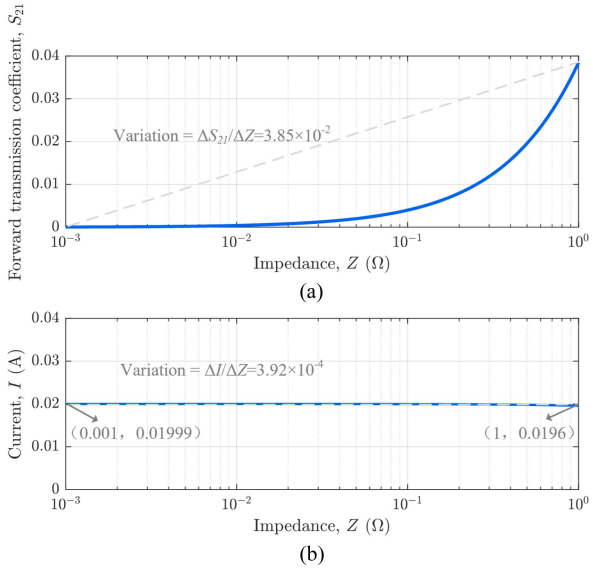

Fig. 4. Theoretical sensitivity analysis of two impedance measurement approaches. (a) Calculated S_{21} for a shunt-through model, demonstrating high sensitivity to impedance variations. (b) Calculated current, *I*, response for an impedance adapter (e.g., the B-WIC model), showing low sensitivity. This theoretical comparison highlights the superior potential of the shunt-through configuration using S_{21} for resolving low impedance values (1 mΩ to 1 Ω).

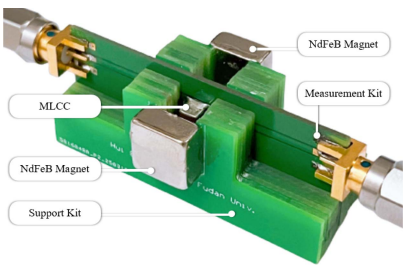

Fig. 5. Measurement kit and setup. NdFeB PMs provide an external *B*-field. A support kit enables adjustable distance between PMs and the MLCC, to control the *B*-field strength. The orientation of PMs determines the *B*-field direction. The PCB design files are provided in the supplementary material.

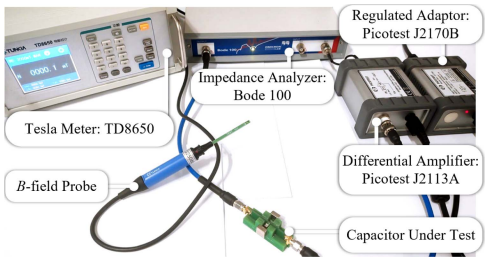

Fig. 6. Measurement test bench. The Bode 100 vector network analyzer measures the impedance of MLCC. The Tesla meter (TD8650) with *B*-field probe monitors the *B*-field magnitude and direction. A Picotest J2113A differential amplifier, powered by a J2170A power supply, is used to suppress ground-loop errors.

explains the advantages of our proposed shunt-through method. The commercial impedance measurement adapter (i.e., B-WIC) has a complex material composition that is vulnerable to the external *B*-field. This vulnerability can invalidate the calibration and makes the measurement results inaccurate. Instead, our fixture is free of ferromagnetic materials, its electromagnetic properties remain constant when the strong magnetic field is applied.

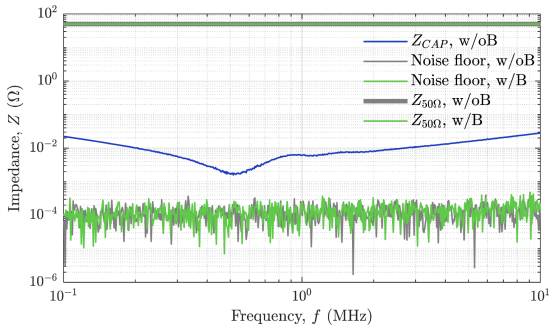

Fig. 7. Impedance versus frequency: MLCC, noise floor, and standard 50 Ω under conditions with and without *B*-field, denoted as w/B and w/o B, respectively. *B*-field application shows negligible effect on noise and 50-Ω impedance, while MLCC impedance remains significantly above the noise floor.

D. Mitigating B-Field Interference on Test Setup

Furthermore, Fig. 2(c) also reveals that the noise floor of a conventional impedance analyzer increases sharply under an external *B*-field. In contrast, the shunt-through method maintains a low noise floor even in the presence of the *B*-field.

E. Experimental Design Kit and Setup

A specialized setup featuring a custom test fixture was developed, as shown in Fig. 3. NdFeB PMs have been used to generate external *B*-fields, thereby avoiding the need for complicated auxiliary circuits. The field strength was precisely controlled by adjusting the distance between the magnets and the device under test (DUT) using a support kit, while the field direction was set by the orientation of the magnets. The overall measurement bench is in Fig. 6.

III. Results

A. Verification of Measurement Accuracy

To validate the measurement system, it is essential to ensure that the background noise is sufficiently low. Fig. 7 presents a comprehensive comparison of the impedance characteristics of the MLCC, the system's noise floor, and a 50 Ω reference resistor. It is evident that the MLCC's impedance is consistently several orders of magnitude above than the system noise floor and proves the accuracy of the system. This large signal-to-noise ratio (SNR) confirms the capability of our setup to accurately measure the MLCC's impedance.

B. Evaluation of B-Field Interference Mitigation

Fig. 8 shows *B*-field distribution along the standard kit. The results verify strong localization of the *B*-field at the DUT, confirming minimal potential interference with the VNA and other sensitive parts of the surrounding setup.

C. Exclusion of Magnet Effects to Confirm B-Field Influence

Because the external *B*-field is introduced using PMs, it is necessary to confirm that any observed effects on DUT originate specifically from the *B*-field, and not from the physical presence or material properties of the magnets.

Fig. 9 presents the impedance of the MLCC measured with an unmagnetized NdFeB magnet, compared to measurements taken without any magnet. The results clearly show that the impedance curves for both conditions ("w/ magnet" and "w/o magnet") are nearly identical. The negligible impedance difference observed with and without this magnet confirms that the physical presence of the material, absent magnetization, does not affect the measurement results.

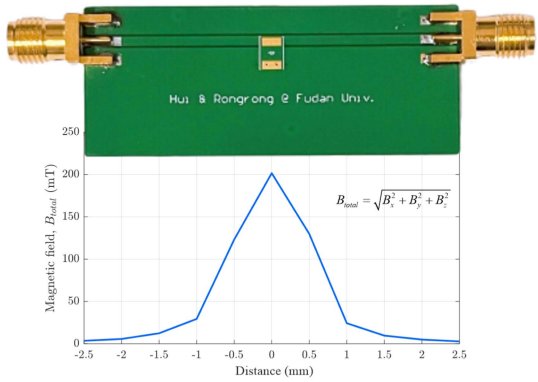

Fig. 8. *B*-field measurements along the standard measurement kit.

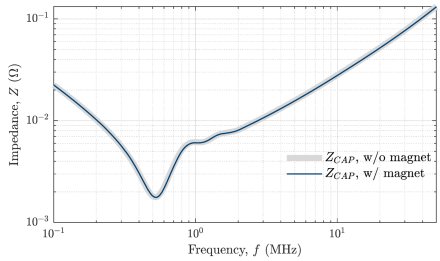

Fig. 9. Impedance measurements versus frequency for the MLCC with and without a magnet, denoted as w/ magnet and w/o magnet, respectively. The nearly identical impedance curves indicate that the presence of the magnet itself, independent of its *B*-field, does not significantly affect the MLCC impedance.

D. Characterization of MLCC Under External B-Field

Fig. 10 shows that the external *B*-field significantly changes the MLCC's impedance, Z, equivalent series inductance, L_s, and equivalent series resistance, R_s. The relative variations are shown in Fig. 10: Z varies from -43.8% to $+32.0\%$, L_s from -72.5% to $+157.7\%$, and R_s decreases by up to 41.0%. Fig. 11 shows a 40.4% decrease in impedance at 800 kHz when the *B*-field is increased from 0 mT to 491 mT. Concurrently, Fig. 12 shows that the first resonant frequency, f_R, increased by 13.2%.

These results in Figs. 8–10 consistently demonstrate the significant impact of external *B*-fields on MLCC performance.

E. Effect of B-Field Polarity on MLCC

To assess the directional dependence, measurements were repeated with reversed *B*-field polarity (N-S versus S-N), as shown in Fig. 13. While the results confirm the significant impact of the *B*-field compared to the no-field case (w/o B), there is negligible difference in the MLCC impedance between the N-S and S-N orientations. This indicates that the observed effects are largely independent of the *B*-field polarity along this axis.

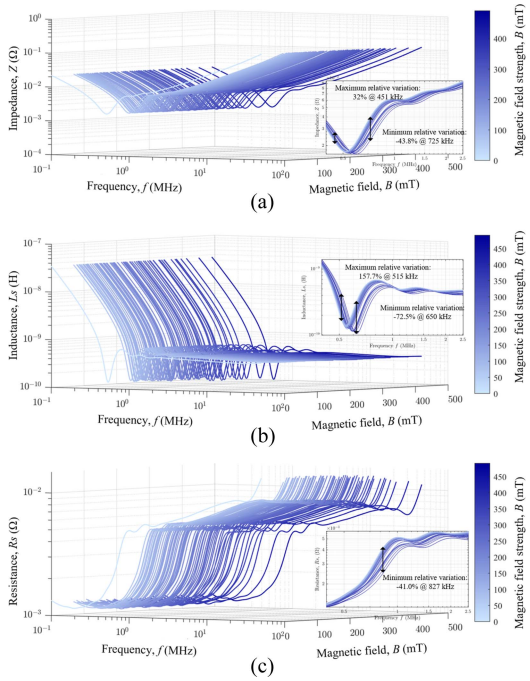

Fig. 10. Effect of applied B-field strength on the parameters of an MLCC (C4532X5R1A107MT000E TDK). Key relative variations include: (a) Impedance, Z: $+32\%$ (max, at 451 kHz) and -43.8% (min, at 725 kHz). (b) Equivalent series inductance, L_s: $+157.7\%$ (max, at 515 kHz) and -72.5% (min, at 650 kHz). (c) Equivalent series resistance, R_s: -41% (min, at 827 kHz).

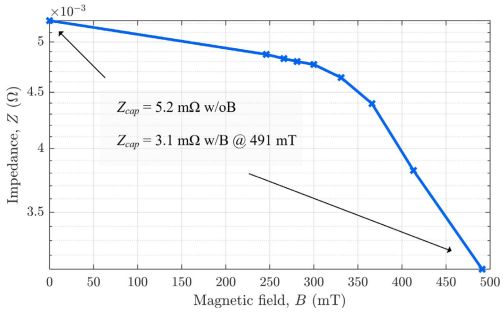

Fig. 11. Impedance of the MLCC at 800 kHz under various B-field strengths. The impedance decreases as the B-field increases. Specific values at $B = 0$ mT and $B = 491$ mT are annotated.

F. Effect of B-Field Orientations on MLCC

As depicted in Fig. 14, the PM is placed in the following nine locations to apply the B-field along key vectors relative to the MLCC.

1) *Along Principal Axes:* Orientations parallel to the x, y, and z axes, which correspond to the B-field applied perpendicularly or parallelly to the MLCC's internal current flow (e.g., positions No. 1, 3, 5, 7, 9).
2) *At 45° Orientations:* Orientations within the principal planes but at a 45° angle to the axes (e.g., positions No. 2, 4, 6, 8).

The results in Fig. 15 clearly show that the B-field's influence on MLCC impedance is a universal phenomenon regardless of orientation. However, the magnitude is affected by orientation, which confirms an anisotropic dependence on orientation.

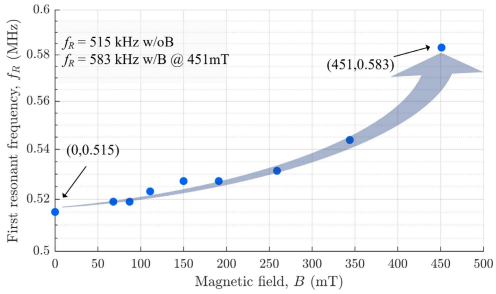

Fig. 12. Measured f_R versus B-field. The f_R is 515 kHz at $B = 0$ mT, while f_R is 583 kHz at $B = 451$ mT. The relative variation of f_R is 13.2%.

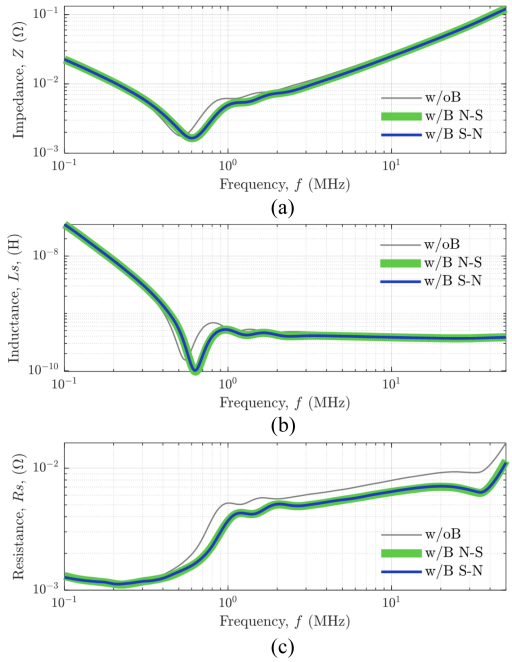

Fig. 13. MLCC parameter variations with frequency and B-field conditions. (a) Impedance. (b) Equivalent Series Inductance, L_s. (c) Equivalent Series Resistance, R_s. Measurements are shown for conditions with and without B-field, denoted as w/B and w/o B respectively. For measurements with B-field, the field was applied in both N-S and S-N directions.

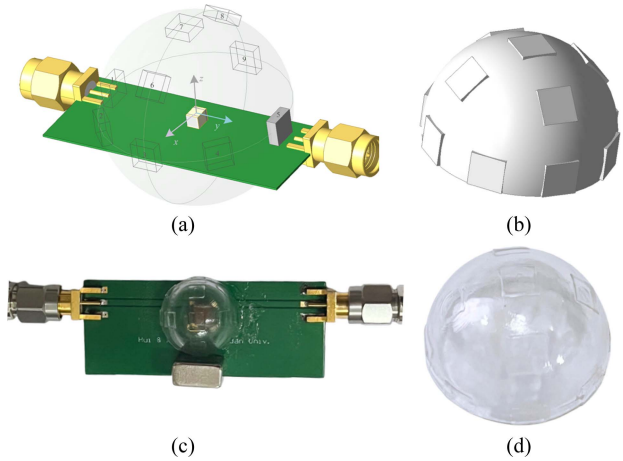

Fig. 14. Design and implementation of the high-precision fixture for PM placement. (a) Schematic of the defined measurement positions, (b) 3-D CAD model of the positioning fixture, (c) photograph of the final assembled test setup, and (d) the fabricated 3-D printed positioning fixture. The designed 3-D CAD model fixtures have been included in the supplemental material.

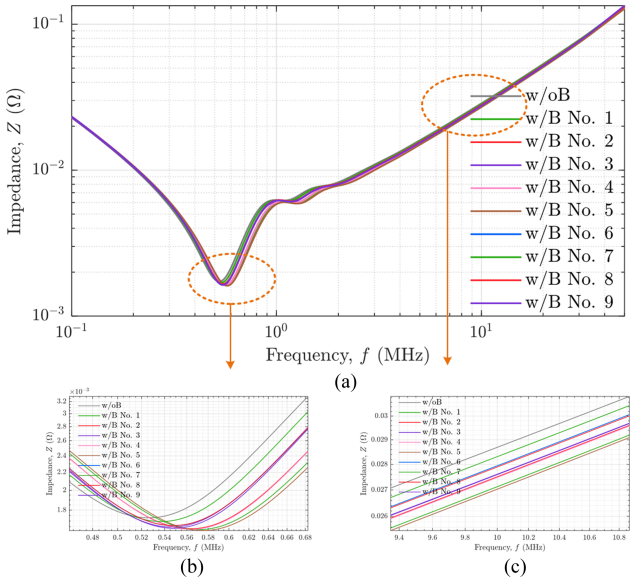

Fig. 15. Measured impedance of the MLCC with and without an external B-field applied at nine positions, measured using the 3-D printed fixture with radius = 5 mm. (a) Full-spectrum impedance curves for all nine magnet positions. (b) A zoomed-in view of the resonant frequency. (c) A zoomed-in view of the high-frequency region around 10 MHz. The results show strong symmetry between corresponding measurement positions.

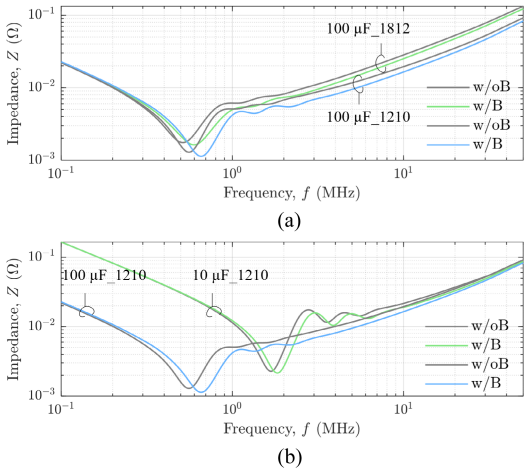

Fig. 16. Measured impedance versus frequency, demonstrating the impact of an external *B*-field (w/B versus w/o B) on (a) 100 μF MLCCs for both 1812 and 1210 package sizes, and (b) 1210 package MLCCs with different capacitance values (100 μF versus 10 μF).

G. Investigation of B-Field Across Various MLCCs

Significant *B*-field-induced impedance variations are observed for 100 μF MLCCs irrespective of package size (1812 versus 1210), as shown in Fig. 16(a). Similarly, significant *B*-field induced impedance changes are evident for 1210 package MLCCs across different nominal capacitance values (100 μF versus 10 μF), as shown in Fig. 16(b). These results demonstrate that the phenomenon is robust and not strictly limited by specific device parameters within the tested configurations.

Fig. 17 presents f_R as a function of capacitance for various MLCCs (differing in capacitance, package size, and manufacturer). The consistently positive vertical error bars, denoting the *B*-field induced increase in f_R, confirm the generality of f_R upshift across a wide range of tested MLCCs.

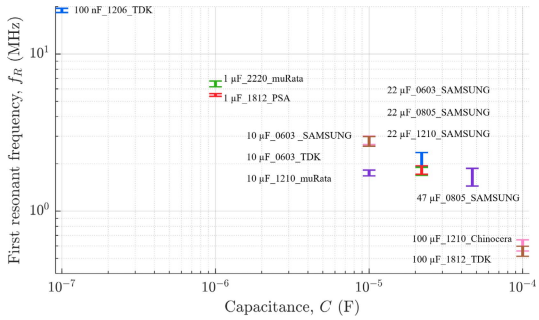

Fig. 17. Measured f_R versus nominal capacitance (C) for various MLCCs. Vertical error bars indicate the increase in f_R upon application of a *B*-field. Each capacitor is identified by its nominal capacitance, package size, and manufacturer (format: Capacitance_Package_Manufacturer). Refer to supplementary information for raw data and further details.

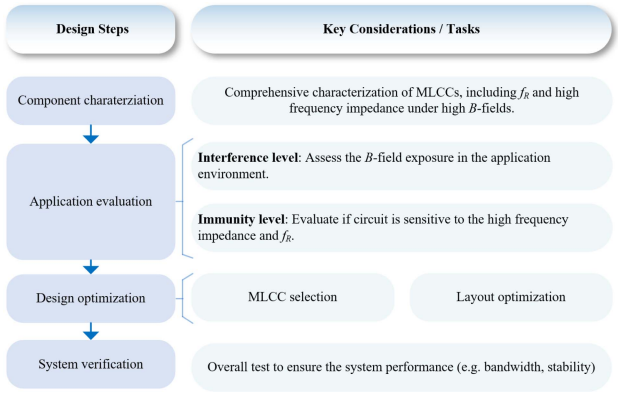

Fig. 18. Design steps and key considerations for applications under high *B*-field environments.

IV. Discussion

The results in Section III clearly shows that high dc *B*-field can cause the MLCCs' high frequency impedance to vary. Therefore, in practical design, we need to evaluate how to include this phenomenon to ensure the performance and high reliability of the system design.

Detailed procedures and key considerations are listed in Fig. 18. For component characterization, refer to the setups in Figs. 5 and 6. For typical interference levels, refer to Table II. It is crucial to identify if the circuits are sensitive to high-frequency impedance changes. Applications such as decoupling capacitors for digital ICs are typically tolerant of an MLCC's high-frequency impedance variations without functional impact. However, circuits with high-bandwidth or stability requirements can be sensitive to MLCC high-frequency impedance. Typical circuits are as follows:

1) *LDO regulators with specific ESR range requirement:* For example, LM1117 [29] requires ESR of the output capacitor is between 0.3 Ω and 22 Ω.
2) *Active EMI filters:* The authors in [30] and [31] used MLCC as the feedback component, C_F. The high frequency impedance variation can affect the bandwidth or stability margin.
3) *Precision Measurement Systems:* Voltage probe architecture incorporating multiple capacitors. When measuring voltages in MagSafe-equipped devices, probe bandwidth

may vary with B-field exposure, potentially affecting measurement accuracy.

This manuscript mainly focuses on the dc B-field effect. Please check the supplementary material for AC B-field analysis.

The primary focus of this manuscript is the effect of dc B-field. While a comprehensive investigation into the underlying root cause is beyond our current scope, we recognize it as a crucial topic for future research. To stimulate and support such investigations, we provide supplementary materials that include a detailed analysis of the ac B-field effect, as well as discussions on the Lorentz force and magnetic modulation effect.

V. Conclusion

The letter reveals a significant phenomenon: External B-field causes substantial variations in the high-frequency impedance parameters of MLCC. We have developed a dedicated experimental setup, including a custom kit, rigorous calibration, and a validated protocol to ensure the reliability, accuracy, and repeatability. Our key findings are summarized as follows:

1) *Significant parameter variation:* We observed significant B-field induced variations: Z ranging from -43.8% to $+32\%$, L_s ranging from -72.5% to $+157.7\%$, R_s decreasing by up to 41%, and f_R increasing by 13.2% at $B = 491$ mT.
2) *Broad applicability:* The observed phenomenon is prevalent across a wide range of MLCCs including both class I (paraelectric) and class II (ferroelectric) capacitors, irrespective of capacitance value, package size, or manufacturer.

References

[1] Y. Jiang et al., "Loss characterization and modeling of class II multilayer ceramic capacitors: A synergistic material-microstructure-device approach," *IEEE Trans. Power Electron.*, vol. 38, no. 11, pp. 13535–13554, Nov. 2023.

[2] J. Li et al., "Grain-orientation-engineered multilayer ceramic capacitors for energy storage applications," *Nature Mater.*, vol. 19, no. 9, pp. 999–1005, Sep. 2020.

[3] J. Xu, L. Gu, and J. Rivas-Davila, "Effect of class 2 ceramic capacitor variations on switched-capacitor and resonant switched-capacitor converters," *IEEE J. Emerg. Sel. Topics Power Electron.*, vol. 8, no. 3, pp. 2268–2275, Sep. 2020.

[4] D. Menzi, D. Bortis, G. Zulauf, M. Heller, and J. W. Kolar, "Novel iGSE-C loss modeling of X7R ceramic capacitors," *IEEE Trans. Power Electron.*, vol. 35, no. 12, pp. 13367–13383, Dec. 2020.

[5] Maximize Market Research, "Multilayer ceramic capacitor market," Maximize Market Research, Mumbai, India, Rep. 28947, Apr. 2025. Accessed: Aug. 2025. [Online]. Available: https://www.grandviewresearch.com/industryanalysis/inductor-market-report

[6] "Inductor market size, share & trends analysis report," Grand View Research, 2024.

[7] S. Coday and R. C. N. Pilawa-Podgurski, "Characterization and modeling of ceramic capacitor losses under large signal operating conditions," *IEEE Open J. Power Electron.*, vol. 4, pp. 24–33, 2023.

[8] D. Menzi, S. Ben-Yaakov, G. Zulauf, and J. W. Kolar, "ESR modeling of class II MLCC large-signal-excitation losses," *IEEE Trans. Power Electron.*, vol. 38, no. 5, pp. 5711–5715, May 2023.

[9] M. S. Alkathy et al., "Enhancing dielectric properties and thermal stability in microwave-synthesized Nd-modified barium titanate nanoceramics for possible MLCC applications," *Appl. Phys. A*, vol. 130, no. 6, May 2024, Art. no. 402.

[10] C. Zhu et al., "Reliability mechanisms of the ultrathin-layered BaTiO3-based BME MLCC," *Acta Physico-Chimica Sinica*, vol. 40, no. 1, Jan. 2024, Art. no. 2304015.

[11] J. W. Lee, H. Song, D.-Y. Jeong, and J. Ryu, "Dielectric and ferroelectric property changes of BaTiO3 ceramics under in-plane stress application," *J. Alloys Compounds*, vol. 1020, Mar. 2025, Art. no. 179404.

[12] J. Pyrhöne, T. Jokinen, and V. Hrabovcová, *Design of Rotating Electrical Machines*, 2nd ed. Chichester, UK: Wiley, 2013.

[13] Y. Yu et al., "Multi objective optimization of permanent magnet synchronous motor based on taguchi method and PSO algorithm," *Energies*, vol. 16, no. 1, 2023, Art. no. 267.

[14] S. J. Seidman, J. Guag, B. Beard, and Z. Arp, "Static magnetic field measurements of smart phones and watches and applicability to triggering magnet modes in implantable pacemakers and implantable cardioverter-defibrillators," *Heart Rhythm*, vol. 18, no. 10, pp. 1741–1744, 2021.

[15] S.-M. Argyri, L. Svenningsson, F. Guerroudj, D. Bernin, L. Evenäs, and R. Bordes, "Contact-free magnetic resonance imaging and spectroscopy with acoustic levitation," *Nature Commun.*, vol. 16, no. 1, Apr. 2025, Art. no. 3917.

[16] B. B. Biswal and L. Q. Uddin, "The history and future of resting-state functional magnetic resonance imaging," *Nature*, vol. 641, no. 8065, pp. 1121–1131, May 2025.

[17] Z. Wang et al., "Equally split PCB inductor (ESPI) design for high energy density and low near-field radiation," *IEEE Trans. Power Electron.*, vol. 39, no. 5, pp. 4963–4968, May 2024.

[18] Y. Lai, S. Wang, and B. Zhang, "Investigation of magnetic field immunity and near magnetic field reduction for the inductors in high power density design," *IEEE Trans. Power Electron.*, vol. 34, no. 6, pp. 5340–5351, Jun. 2019.

[19] H. Zhang and S. Wang, "Near magnetic field assessment and reduction for magnetic inductors with magnetic moment analysis," *IEEE Trans. Power Electron.*, vol. 37, no. 2, pp. 1641–1652, Feb. 2022.

[20] J. Garnica, R. A. Chinga, and J. Lin, "Wireless power transmission: From far field to near field," *Proc. IEEE*, vol. 101, no. 6, pp. 1321–1331, Jun. 2013.

[21] Y. Shao, M. Liu, and C. Ma, "A multi-receiver MHz WPT system with hybrid coupler," in *Proc. IEEE PELS Workshop Emerg. Technol.: Wireless Power Transfer*, Jun. 2021, pp. 1–6.

[22] J. Kim et al., "Coil design and shielding methods for a magnetic resonant wireless power transfer system," *Proc. IEEE*, vol. 101, no. 6, pp. 1332–1342, Jun. 2013.

[23] R. Zhang et al., "Using 2-D core and origami winding to push the first resonant frequency of nanocrystalline common-mode inductors beyond 10 MHz with improved performance," *IEEE Trans. Power Electron.*, vol. 39, no. 10, pp. 11997–12002, Oct. 2024.

[24] M. Vasic, J. A. Oliver, P. Alou, J. A. Cobos, and P. J. Grbovic, "Experimental evaluation of capacitors for high power resonant converters," in *Proc. PCIM Europe 2017; Int. Exhib. Conf. Power Electron., Intell. Motion, Renewable Energy Energy Manage.*, May 2017, pp. 1–6.

[25] D. Neumayr, D. Bortis, J. W. Kolar, M. Koini, and J. Konrad, "Comprehensive large-signal performance analysis of ceramic capacitors for power pulsation buffers," in *Proc. IEEE 17th Workshop Control Model. Power Electron.*, Jun. 2016, pp. 1–8.

[26] C. B. Barth, T. Foulkes, I. Moon, Y. Lei, S. Qin, and R. C. N. Pilawa-Podgurski, "Experimental evaluation of capacitors for power buffering in single-phase power converters," *IEEE Trans. Power Electron.*, vol. 34, no. 8, pp. 7887–7899, Aug. 2019.

[27] D. Zakzewski, Y. Shen, A. Hasnain, R. Resalayyan, and A. Khaligh, "Class II ceramic capacitor voltage characteristic modeling and compensation for AC-connected applications," *IEEE J. Emerg. Sel. Topics Ind. Electron.*, vol. 5, no. 4, pp. 1582–1592, Oct. 2024.

[28] J. Antony, *Design of Experiments for Engineers and Scientists*. Oxford, UK: Elsevier, 2022.

[29] "LM1117 800-mA, low-dropout linear regulator," Texas Instruments, Dallas, TX, USA, Datasheet, 2023. Accessed: Aug. 2025. [Online]. Available: https://www.ti.com/lit/ds/symlink/lm1117.pdf

[30] R. Goswami and S. Wang, "Investigation and modeling of combined feedforward and feedback control schemes to improve the performance of differential mode active EMI filters in AC–DC power converters," *IEEE Trans. Ind. Electron.*, vol. 66, no. 8, pp. 6538–6548, Aug. 2019.

[31] Y. Zhou et al., "A novel virtual capacitance enhancement-based active EMI filter for CM noise attenuation," *IEEE Trans. Ind. Electron.*, vol. 71, no. 12, pp. 16870–16874, Dec. 2024.